JOURNAL OF CATALYSIS 152, 164–178 (1995)

Particle and Phase Thicknesses from XPS Analysis of Supported Bimetallic Catalysts: Calcined Co–Rh/Nb_2O_5

A. Frydman,*,‡ D. G. Castner,† M. Schmal,‡ and C. T. Campbell*,[1]

*Department of Chemistry, BG-10, University of Washington, Seattle, Washington 98195; †Department of Chemical Engineering, BF-10, University of Washington, Seattle, Washington, 98195; and ‡NUCAT/COPPE/PEQ, Universidade Federal do Rio de Janeiro, CP 68502, CEP 21945, Ilha do Fundão, Rio de Janeiro, Brazil

Received May 23, 1994; revised November 7, 1994

The surface structure and elemental composition of a series of calcined Co–Rh/Nb_2O_5 bimetallic catalysts have been investigated using X-ray photoelectron spectroscopy (XPS) and temperature-programmed reduction (TPR). New formulae for the quantitative analysis of XPS intensities for supported bimetallic catalysts involving up to three separate, layered phases on spherical support particles are used for the first time. These apply an average take-off angle for photoelectrons from spherical particles whose radii are large compared to the electron attenuation length. Calcined monometallic Co/Nb_2O_5 and Rh/Nb_2O_5, and four calcined bimetallic Co–Rh/Nb_2O_5 catalysts with similar Co loadings (≈ 1.9 wt%) and variable Rh loadings (0.3 to 2.3 wt%) were examined. Reference spectra for pure $CoNb_2O_6$ (columbite) are also presented here for the first time. The catalysts were prepared by incipient wetness impregnation and calcined at 673 K to generate the oxide precursors. The XPS lineshapes and the Co (2p) spin-orbit splitting indicated the presence of two Co species, Co_3O_4 and Co^{+2}, on all calcined Co-containing catalysts. The measured XPS Co/Nb and Rh/Nb atomic ratios for the catalysts were factors of 1.5–2 and 2–4.5, respectively, greater than the bulk atomic ratios, showing that both Co and Rh oxides were surface-enriched. The measured XPS peak intensities were compared to the values predicted from several different structural models of the oxide particles. These models assumed large spherical Nb_2O_5 particles (diameter ≈60 nm to match the BET area) with the Co and Rh oxides covering fractions of this support's surface in several particle arrangements. The best agreement, according to the minimum least squares criteria, was found for a model in which the Co^{+2} phase is adsorbed on the Nb_2O_5 support surface, whereas the Co_3O_4 forms thick (>2.5 nm) islands covered by Rh_2O_3 on ≈3.6% of the support surface. The thickness of the Rh_2O_3 overlayer increased to 2.6 nm as the Rh/Co bulk atomic ratio increased to 0.72. The Co^{+2} phase was present at submonolayer concentrations. Between 78 and 90 mole% of the total Co was present as Co_3O_4 in this model. The reduction temperature of the Co_3O_4 strongly decreased as the Rh/Co bulk atomic ratio increased, while the reduction temperature of the Rh_2O_3 was not strongly influenced by the presence of Co_3O_4. Thus, the TPR results are consistent with this bilayer island model, with Rh_2O_3 on top of Co_3O_4. The Co^{+2} species was not obvious in TPR due to its low concentration.

1. INTRODUCTION

Cobalt-based catalysts have been widely used for the production of hydrocarbons from synthesis gas because of cobalt's intrinsic ability to hydrogenate dissociated carbon species and promote chain growth [1]. Recently, oxygenate formation from synthesis gas has been intensively studied to develop alternate routes of producing fuel additives and chemical feedstocks. Rhodium has attracted strong attention in this regard due to its high efficiency for C_2 oxygenates formation (2, 3), but unfortunately exhibits low selectivities for higher oxygenates (4). Despite its known activity in the CO/H_2 reaction, Co does not show appreciable selectivities for oxygenates (1). Addition of promoters has been frequently used in traditional CO hydrogenation catalysts to improve catalytic activity, selectivity (for hydrocarbons in the gasoline/diesel range, low molecular weight olefins, or C_{2+} oxygenates), and resistance to deactivation by carbonaceous deposits (5–7). For these reasons, several supported bimetallic Co-containing catalysts have been studied (8–16).

The properties of Co catalysts in CO hydrogenation also depend on the support material involved (17–20) and on the nature of surface species formed after the catalyst preparation (21–23). Correlations between the surface composition of the cobalt catalysts (e.g., Co oxidation state) and CO hydrogenation activity have been observed (21–25). It is known that calcination of Al_2O_3 impregnated with a Co^{+2} salt precursor (such as cobalt nitrate) results in the formation of three main Co species: bulk Co_3O_4, Co^{+2} ions in tetrahedral sites ("surface-like spinels") and Co^{+2} ions in octahedral sites (23, 26–28). The relative distribution of these species on the surface is dependent on the cobalt content and calcination temperature (27, 28). Low Co concentrations (below 2%) typi-

[1] To whom correspondence should be addressed.

0021-9517/95 $6.00

cally result in a well-dispersed surface phase (Co^{+2} ions in tetrahedral sites), having features similar to $CoAl_2O_4$, which is difficult to reduce or sulfide (28 and references therein). High Co concentrations typically form a phase consisting of Co_3O_4 crystallites that can be easily reduced or sulfided (28 and references therein). Increasing calcination temperatures favor the formation of the Co^{+2} ions in tetrahedral sites of the support (27). The third known Co species (Co^{+2} ions in octahedral sites) was suggested to be "*surface CoO.*" This species is difficult to reduce, but can be readily sulfided and may contribute to the activity of hydrodesulfurization (HDS) catalysts (29). This third phase has been distinguished from the inert Co^{+2} phase by combining a sulfidation treatment with X-ray photoelectron spectroscopy (30). Such difficult to reduce Co species might play an important role in altering the activity and selectivity for the CO/H_2 reaction. For example, higher CO hydrogenation activities (22–25) and C_{5+} selectivities (22) have been reported for Co catalysts after incomplete reduction, relative to more fully reduced Co catalysts. Higher selectivities for low olefins (31) and C_2 oxygenates (32–34) were found in poorly reduced Co catalysts compared to the more fully reduced state. However, there seems to be an optimum concentration for these unreduced Co species, above which the favorable catalytic features are blocked (23, 33).

Addition of noble metals (known for having considerable hydrogen storage capacity) to Co catalysts can considerably affect the reduction of Co oxides and the ratio of unreduced Co to metallic Co. A few studies have been done with Co–Rh catalysts (12–16). These are possible candidates for obtaining higher CO hydrogenation activities and better oxygenate selectivities since they combine the chain growth ability of Co with the ability of Rh to adsorb CO either molecularly or dissociatively (35, 36). Increasing ethanol and propanol selectivities have been reported for bimetallic $Co–Rh/TiO_2$ in comparison to the monometallic Co/TiO_2 and Rh/TiO_2 (13). Also, a few studies of CO hydrogenation over supported metal catalysts using Nb_2O_5 as the support material have been recently published (37–43). These have reported that the use of Nb_2O_5 as a support results in better CO hydrogenation activities for Rh/Nb_2O_5 in comparison to Rh supported on ZrO_2, Al_2O_3, SiO_2, or MgO (41), and for Ni/Nb_2O_5 in comparison to Ni/SiO_2 (42). Enhancement in selectivity for high molecular weight hydrocarbons in CO hydrogenation over Co/Nb_2O_5 (37, 38) and Ni/Nb_2O_5 (43) compared to more traditional supports (Al_2O_3 (37, 38, 43) and SiO_2 (38)), was also observed.

In this study, we characterize a series of calcined $Co–Rh/Nb_2O_5$ catalysts using X-ray photoelectron spectroscopy (XPS). A detailed structural model for these calcined catalysts which is quantitatively consistent with the XPS data and with temperature-programmed reduction (TPR) features is also developed. These results will be correlated to the activity and selectivity of these catalysts for CO hydrogenation in a future publication (44).

The XPS signals expected from various structural models are calculated here using a new mathematical formalism (64) for the first time. This formalism is appropriate for random or spherical particles whose radii are large compared to the photoelectron attenuation length, and it specifically considers the variation in photoelectron take-off angle over the front hemispherical surface of the particles. It is similar to the "randomly oriented hemispheres model" of Kuipers *et al.* (65), except that it is applicable also to layered phases on the support, such as frequently occurs in bimetallic catalysts. A simpler approximation to this formalism, using an average take-off angle of photoelectrons from the local surface normal of 57.3°, is shown to be sufficient for optimizing structural parameters in bimetallic catalysts like these.

Characterizations of a reference cobalt niobate ($CoNb_2O_6$) by XPS is also presented here.

2. EXPERIMENTAL

2.1. Catalyst Preparation

The support material obtained from CBMM (Companhia Brasileira de Metalurgia e Mineração) was originally niobic acid AD399 (99.8% purity and surface area of 95 m^2/g), one of the natural states of niobium. The supplier of the support provided the following analysis of impurities on the original material : Ta (1580 ppm), Si (370 ppm), Ti (70 ppm), Na (50 ppm), K (95 ppm), and Fe (60 ppm). After calcination at 873 K for 4 h, the original material is converted from an amorphous phase to the crystalline TT or T form of niobium pentoxide (45). Under these conditions, Nb_2O_5 is a macroporous material (pores larger than 50 nm) with a surface area of 25 m^2/g.

The catalysts were prepared by conventional incipient wetness impregnation and the bimetallics were prepared by coimpregnation. The cobalt and rhodium precursors were $Co(NO_3)_2 \cdot 6H_2O$ (Riedel-de Häen, 99% purity) and $Rh(NO_3)_3$ (Aldrich, solution in 10–15% HNO_3, Rh content 10%), respectively. Cobalt content was kept approximately constant (ca. 1.9 wt%) and the Rh/Co bulk atomic ratio for the bimetallic catalysts varied from 0.09 to 0.72. After the impregnation, the catalysts were dried overnight at 383 K and calcined at 673 K for 4 h.

Reference compounds Co_3O_4, Rh_2O_3 and $CoNb_2O_6$ were also prepared. The Co_3O_4 was obtained by calcination of the cobalt nitrate precursor at 673 K for 4 h. The rhodium nitrate precursor solution was carefully evaporated overnight at 323 K and the residual was calcined at 673 K for 4 h to obtain the Rh_2O_3. The $CoNb_2O_6$ precursor was prepared by pH-controlled titration of a solution

TABLE 1

Bulk Concentration and Surface Area of Calcined Co–Rh/Nb_2O_5 Catalysts

Sample	(wt%)[a] Co	Rh	Atomic ratio[a] Rh/Co (bulk)	BET area (m^2/g)
Co/Nb	1.9	—	—	29
Rh/Nb	—	0.85	—	29
Co09Rh/Nb	2.0	0.31	0.09	22
Co19Rh/Nb	1.85	0.60	0.19	26
Co24Rh/Nb	1.75	0.73	0.24	22
Co72Rh/Nb	1.85	2.33	0.72	20

[a] From atomic absorption.

of $K_2Nb_2O_6$ (solute obtained from CBMM) with a solution of $Co(NO_3)_2 \cdot 6H_2O$ following the methodology described elsewhere (46). The precipitate precursor was dried overnight at 383 K and calcined at 893 K for 2 h. Under these conditions, the columbite structure of the cobalt niobate forms, albeit with poor crystallinity (small crystal size, or broad peaks in XRD) (46).

2.2. *Characterization*

Cobalt and rhodium bulk concentrations were measured by atomic absorption (AA) using a calibration curve of a standard solution of cobalt or rhodium nitrates. Surface areas were measured by the conventional BET method using N_2. The characterization of the catalysts is summarized in Table 1.

The stoichiometry of the supported oxides as well as the interactions between those phases and the support material were studied with TPR by flowing hydrogen over the calcined sample and heating at 8 K/min from 293 to 1173 K. Hydrogen consumption was monitored by a thermal conductivity detector. Further details about the TPR technique applied to the present work will be published in a future report (44). Only qualitative results of the TPR experiment will be described here, to supplement the XPS results presented in this study.

Surface composition and structure of the catalysts were analyzed by XPS using a Surface Science Instruments (SSI) X-probe spectrometer. This system has a cryopumped UHV analysis chamber, a variable X-ray spot size with an elliptical area whose short axis can be adjusted to 150, 300, 600, or 1000 μm, a monochromatic Al($K\alpha$) X-ray source, a hemispherical electron analyzer with variable pass energies of 25, 50, 100, and 150 eV, a large acceptance angle (30° solid angle) analyzer lens system with a variable aperture assembly, a multichannel detection system, a charge neutralization system, a turbopumped sample introduction chamber, and a computer-controlled x-y-z translation and rotation sample manipulator. The X-Probe is controlled by an HP-9836C computer system. The software on this system was also used to determine the elemental surface composition and to peak-fit the high-resolution spectra. A sample holder for the catalyst powders was prepared by machining eight holes 1 mm deep and 8 mm in diameter into the face of a standard 5-cm diameter sample stage. A few milligrams of powder was placed in each hole and then gently pressed using an 8-mm diameter, tungsten carbide tipped punch to produce a pellet with a smooth surface. This procedure was used for all Nb_2O_5 supported catalysts and Co_3O_4. The $CoNb_2O_6$ and Rh_2O_3 powders did not produce a suitable pellet under these conditions. The $CoNb_2O_6$ and Rh_2O_3 powders were pressed into freshly scraped In foil for analysis. For all Nb-containing samples, charge neutralizations was required. This was accomplished by using 2 eV electrons directed at the samples from a low-energy electron flood gun. An electrically grounded, 90% transmission Ni mesh was then mounted $\approx$2 mm above the samples to improve charge neutralization (47).

For all samples, first a survey spectrum over the photoelectron binding energy (B.E.) range of 0 to 1000 eV was acquired using an analyzer pass energy of 150 eV and an X-ray spot size of 1000 μm. From this survey scan, all the elements present in the surface region (ca. outer 50 Å) at the concentration above a few tenths of an atomic percent were identified. Next, scans covering the regions of characteristic peaks for each element (Nb (3d), Rh (3d), Co (2p), O (1s), and C (1s)) were done at a pass energy of 150 eV and an X-ray spot size of 1000 μm for determination of surface elemental compositions. The area under the photoelectron peaks was measured and normalized by the analysis time per point, the number of points per eV, and the analyzer transmission function. To calculate "surface atomic ratios" from these XPS intensities, they were further normalized to their reported photoelectron mean free paths (λ) (48) and photoionization cross sections (σ) (49). In addition to the main elements present in the samples (Nb, Co, Rh, O), the XPS results also detected the presence of minor amounts of C ($\approx$14 atom% in the XPS probe depth). The transmission function of the SSI spectrometer is constant versus kinetic energy for an analyzer pass energy of 150 eV (50). The spectrometer absolute B.E. scale was calibrated to the known value for the ($4f_{7/2}$) peak of a pure gold reference (B.E. of 83.93 eV). The linearity of the B.E. scale was calibrated to the known B.E. splitting between the Cu (3s) and the Cu ($2p_{3/2}$) peaks of a pure metallic copper reference (B.E. splitting of 810.08 eV).

In addition to surface elemental composition, high-resolution spectra were obtained for the Rh (3d), Co (2p),

and Nb (3*d*) peaks to provide lineshape information. For the Rh and Nb spectra, an analyzer pass energy of 50 eV and an X-ray spot size of 1000 μm was used. Unlike the Rh and Nb (3*d*) peaks, decreasing the analyzer pass energy from 150 to 50 eV did not produce a significant narrowing for the Co (2p) peaks from the supported catalysts, so an analyzer pass energy of 150 eV was used for Co (2*p*) peaks, thus giving higher count rates. The B.E.s and peak areas of the various species present in each spectrum were then determined using the peak fitting software.

3. RESULTS

3.1. TPR

The TPR spectra of the Co/Nb catalyst exhibited two peaks of hydrogen consumption at 655 and 787 K, with stoichiometries consistent with two steps of reduction: $Co_3O_4 + H_2 \Rightarrow 3\ CoO + H_2O$ and $3\ CoO + 3\ H_2 \Rightarrow 3\ Co^0 + 3\ H_2O$. These steps have been previously detected (16, 28, 51–53). This observation is consistent with Co_3O_4 as the main form of cobalt after calcination. The Rh/Nb catalyst had stoichiometry and temperature of reduction (367 K) consistent with the reduction of Rh_2O_3 to metallic Rh (16). The lineshapes of the bimetallic samples suggested an intimate contact between cobalt and rhodium phases after the oxidation treatment, since their reduction profiles are not a superposition of the monometallic profiles. Specifically, the Co_3O_4 in the bimetallic catalysts was reduced at substantially lower temperatures when Rh was present, and the Co_3O_4 and CoO were simultaneously reduced in a single TPR peak. The reduction temperature of this peak decreased with increasing Rh content of the bimetallic catalysts (545 K for the Co72Rh/Nb sample). This shows that the presence of Rh strongly influences the reduction of the Co oxide. The bimetallic catalysts showed a TPR peak which shifted from 363 to 419 K as the Rh loading increased. These sharp peaks were quite similar in shape and reduction temperature to Rh_2O_3 in the monometallic Rh/Nb catalyst (367 K) (44) and in the pure Rh_2O_3 sample (408 K) (16). Thus, the addition of Co has no clear influence on the reduction behavior of the Rh_2O_3 phase, or at least the influence is not significantly greater than that due to the Nb_2O_5 support. In all the catalysts, there was some excess H_2 consumption, suggesting partial reduction of the support or hydrogen spillover onto or into the support. In summary, the TPR spectra of the bimetallic samples strongly suggested Co_3O_4 and Rh_2O_3 were the predominant oxidic forms of Co and Rh, respectively, on the catalysts. Indeed, these are the most stable oxidation states of these pure elements under our calcination conditions (54). These two forms have also been suggested as the main oxidic forms in other calcined Co–Rh catalysts on Al_2O_3 and TiO_2 (16).

3.2. XPS

3.2.1. Lineshapes and binding energies. Figures 1 and 2 show the XPS lineshapes of Co (2*p*) and Rh (3*d*) spectra, respectively, of the different calcined catalysts and the reference pure compounds Co_3O_4, Rh_2O_3, and $CoNb_2O_6$. The Nb ($3d_{5/2}$) line, set to a binding energy (B.E.) of 207.4 eV (55), was used as a binding energy reference for the catalysts. The pure Co_3O_4 and Rh_2O_3 standards required no correction since they had sufficient conductivity to be analyzed without the flood gun. The reported Nb ($3d_{5/2}$) B.E. of 206.5 eV (55a) for $RhNbO_4$ was used as a binding energy reference for our $CoNb_2O_6$ sample, thereby assuming that these two niobates have the same Nb ($3d_{5/2}$) B.E..

The Co (2*p*) lineshapes of the catalysts suggest the presence of two different Co species on the surface. This is more obvious from the large width and unresolved doublet structure apparent in the Co ($2p_{1/2}$) peak. The broadening in the Co ($2p_{3/2}$) peak is not as obvious. This, we believe, is because the energy separation between the Co ($2p_{3/2}$) peak and the Co ($2p_{1/2}$) peak is close to 15.2 eV for Co_3O_4, but substantially larger for pure Co^{+2} oxides, like $CoNb_2O_6$ (≈15.9 eV), as shown in Table 2. Our results are in excellent agreement with spin–orbit splitting val-

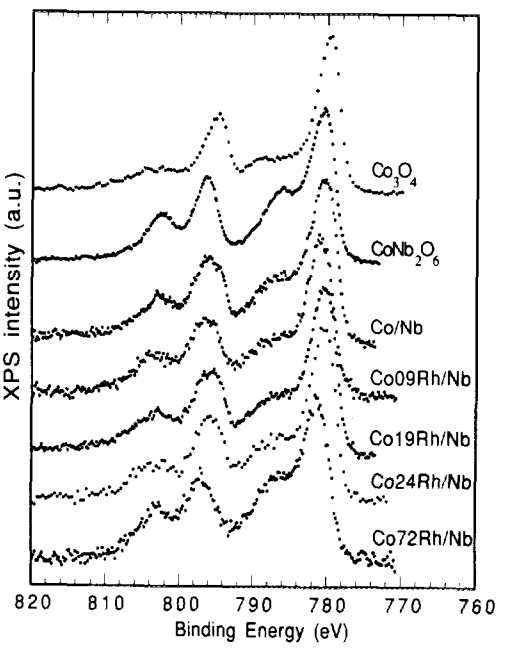

FIG. 1. Co(2*p*) spectra of the calcined Co–Rh/Nb_2O_5 catalysts and the pure reference compounds, Co_3O_4 and $CoNb_2O_6$. All spectra were scaled to the same peak intensity, and energy referenced as described in text. (Pass energy = 150 eV.)

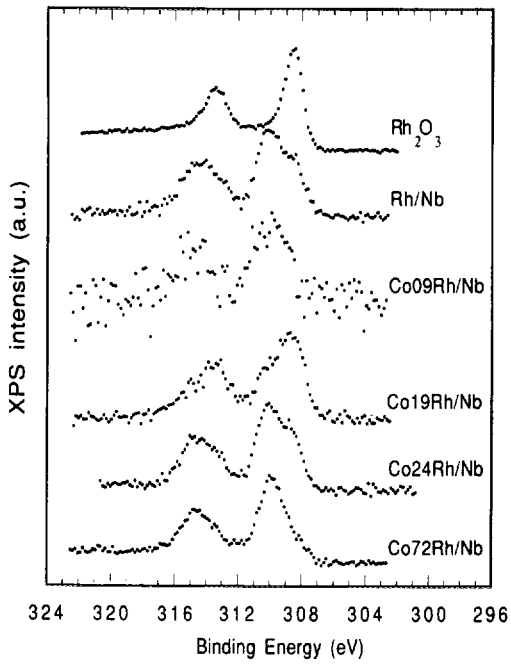

FIG. 2. Rh(3*d*) spectra of the calcined Co–Rh/Nb_2O_5 catalysts (pass energy = 50 eV) and the pure reference compound, Rh_2O_3 (pass energy = 25 eV). All spectra were scaled to the same peak intensity, and energy referenced as described in text.

ues for pure Co_3O_4 (15.0 eV (10c, 56a)) and for pure CoO (15.5 eV (10c, 56b) and 15.9 eV (56a)). The broadening of the Co ($2p_{1/2}$) line in our catalysts therefore suggests a superposition of Co_3O_4 and Co^{+2} oxide features. The TPR suggests most of the Co is in the Co_3O_4 form, but the surface composition clearly has a comparable amount of Co^{+2} oxide. As we will see below, this is because the Co^{+2} phase is dispersed over the Nb_2O_5 surface, whereas the Co_3O_4 is in particles on the surface of the support and covered by a Rh oxide phase. The surface sensitive nature of XPS emphasizes the dispersed Co^{+2} phase (21).

Figure 3 shows how the Co (2*p*) lineshapes of the catalysts were resolved into contributions from Co_3O_4 and Co^{+2} features. In Fig. 3a, the Co (2*p*) spectrum of the calcined Co/Nb catalyst is compared to a scaled Co (2*p*) spectrum of the pure Co_3O_4. The difference between these two spectra is shown in Fig. 3b, and compared to a scaled Co (2*p*) spectrum of a pure $CoNb_2O_6$. It is clear that the difference spectrum is essentially identical to the $CoNb_2O_6$ reference spectrum. Similarly, all the catalysts' Co (2*p*) spectra were well fit by a simple superposition of Co_3O_4 and Co^{+2} (specifically $CoNb_2O_6$) features. (In this fitting procedure, shifts by up to 1.0 eV in the catalysts spectra were needed in some cases, presumably due to charging problems.) The relative intensities of the Co_3O_4 and Co^{+2} spectra needed for the best fits are plotted in Fig. 4 as a function of Rh content. The error bars in this fitting ratio, $I_{Co_3O_4}/I_{Co^{+2}}$, are rather large (±35%). (This error basically represents the uncertainty of the procedure used to resolve the Co (2*p*) XPS spectra in two parts and to fit these parts to the Co (2*p*) XPS spectra of pure references Co_3O_4 and $CoNb_2O_6$.) The relative Co_3O_4 XPS signal is clearly lower at the highest Rh content. As we will see below, this is because the Co_3O_4 XPS signal is attenuated by the thick Rh oxide phase on top of it in this

TABLE 2

Measured Binding Energies of the Main Elements in the Calcined Co–Rh/Nb_2O_5 Catalysts and Reference Compounds

	Binding energy of the elements (in eV)								
Sample	Nb($3d_{5/2}$)	O(1*s*)	C(1*s*)	Co($2p_{3/2}$) main	Co($2p_{3/2}$) satellite	Δ B.E. Co ($2p_{1/2}$–$2p_{3/2}$)	Rh($3d_{5/2}$) high	Rh($3d_{5/2}$) low	Ref.
Co/Nb	207.4	530.2	285.2	780.5	786.7	15.4	—	—	
Rh/Nb	207.4	530.3	285.2	—	—	—	310.2	308.6	
Co09Rh/Nb	207.4	530.4	285.1	780.8	786.9	15.4	310.2	308.7	
Co19Rh/Nb	207.4	530.3	285.2	780.3	786.4	15.4	310.3	308.5	
Co24Rh/Nb	207.4	530.3	284.9	780.4	786.3	15.4	310.2	308.6	
Co72Rh/Nb	207.4	530.4	285.1	780.8	786.4	15.6	310.1	308.9	
Nb_2O_5									
present study	207.4	530.3	285.2	—	—	—	—	—	
literature	207.4	530.4[a]	—	—	—	—	—	—	(55)
Co_3O_4									
present study	—	529.5	284.4	779.7	786.1	15.2	—	—	
literature	—	529.5	—	779.9	—	—	—	—	(55b,56)
Rh_2O_3									
present study	—	530.3	284.1	—	—	—	308.5		
literature	—	530.6	—	—	—	—	308.5		(55a,57)
$CoNb_2O_6$	206.5	529.7	285.0	780.5	785.9	15.9	—	—	

[a] From (55a), corrected to reference B.E. of 207.4 eV for Nb($3d_{5/2}$) based on the average of references (55a–i).

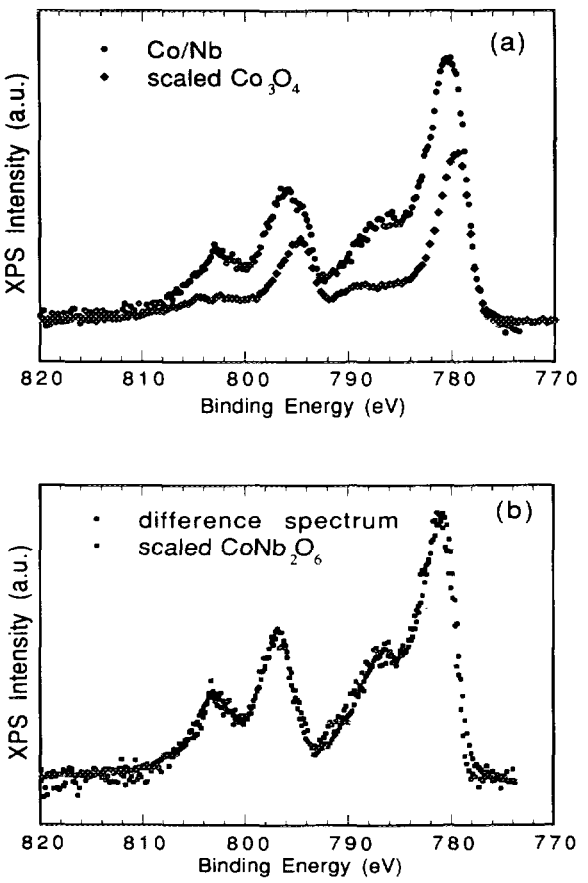

FIG. 3. Comparisons of Co (2*p*) spectra between the calcined Co/Nb catalyst and the pure reference compounds, Co_3O_4 and $CoNb_2O_6$. (a) Spectrum of the calcined Co/Nb catalyst and of the pure Co_3O_4, scaled by a factor of 1.75 and slightly shifted, to obtain the greatest overlap of the low B.E. edges of these. (b) Difference spectrum obtained from the peaks in (a), plotted for comparison to the spectrum of pure $CoNb_2O_6$. The later spectrum was scaled by a factor 0.52 to obtain agreement in total intensity.

sample. The Co^{+2} phase, in contrast, will be shown to be a monolayer-dispersed surface phase on the Nb_2O_5 support, not covered by other species. Since the lineshape of other Co^{+2} oxides like CoO (10c, 56b) are very similar to that of $CoNb_2O_6$, we cannot definitively determine whether the Co^{+2} species detected on the supported catalysts is Co niobate or another Co^{+2} oxide.

The Rh (3*d*) lineshape was not very useful for clarifying the Rh environment. This is because this lineshape changed with time during measurement. Both the $3d_{5/2}$ and $3d_{3/2}$ peaks showed a doublet structure, with a splitting of ≈1.5 eV between the higher binding energy and lower binding energy features, which were located at ≈310.2 and 308.7 eV, respectively, for the $3d_{5/2}$ peak (see Table 2). The intensity of the lower B.E. feature grew with measurement time at the expense of the higher B.E. feature. We tentatively attribute this to reduction of Rh_2O_3, due to effects of the X-ray beam and/or reaction with background-gases. The splitting of ≈1.5 eV compares to a splitting of 1.5 eV in the average of reported B.E.s for pure Rh_2O_3 and pure Rh metal, which are at 308.5 eV (55a, 57) and 307.0 eV (56b, 57a, 58), respectively, for the Rh ($3d_{5/2}$) line. As we will see below, the Rh oxide exists as a thin (0.6–3.1 nm) film on the surface of the catalyst, so it should be very susceptible to changes due to surface reactions. In contrast, no changes in the Rd (3*d*) peak lineshape with time was detected for the unsupported Rh_2O_3 powder. Unlike the Rh features, the Nb and Co XPS features were stable with time on both supported and unsupported samples. We attribute the higher B.E. Rh ($3d_{5/2}$) feature to Rh_2O_3 mainly because our TPR results show that the Rh reduction closely resembles that of Rh_2O_3 in temperature, lineshape, and stoichiometry (16, 44), and not because of its binding energy. Indeed, its B.E. of ≈310.2 eV disagrees with the average of reported values for pure Rh_2O_3 (308.5 eV (55a, 57)). We speculate that this shift of ≈1.7 eV in the Rh (3*d*) peaks is due to differential charging. The Rh phase is partially reduced in UHV. Metallic Rh could have a higher secondary electron emission coefficient than oxides, thus leading to greater positive charge buildup and higher apparent B.E. values in the Rh phase. Further experiments are required to resolve this issue.

3.2.2. XPS Signal Intensities. Table 3 shows the experimental XPS intensities ratios for Co/Nb, Rh/Nb, and Rh/Co. The Co, Rh, and Nb intensities referred to here

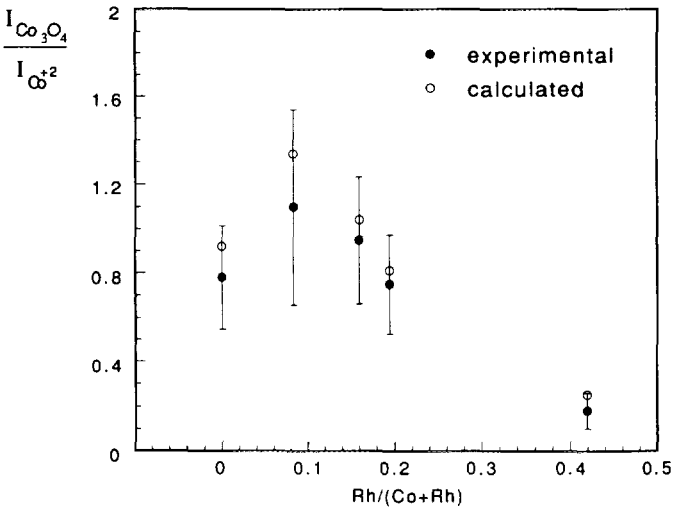

FIG. 4. Ratio of the Co ($2p_{3/2}$) XPS intensity in the Co_3O_4 phase to that in the Co^{+2} phase, plotted as a function of the Rh content in the catalyst (on an atomic ratio basis). The experimental values have been assigned error bars based on the inaccuracies in assessing the relative Co_3O_4 and Co^{+2} signals by the lineshape fitting procedure shown in Fig. 3. The calculated values refer to our preferred model, as described in text, employing the full angular integration method of Eq. [1c].

TABLE 3

Experimental XPS Intensities Ratios for the Calcined Co-Rh/Nb_2O_5 Catalysts, and Parameters Used in Quantitative Analysis

Sample	Bulk atomic ratio			Experimental XPS intensity ratio			XPS atomic ratio		
	Co/Nb	Rh/Nb	Rh/Co	Co/Nb	Rh/Nb	Rh/Co	Co/Nb	Rh/Nb	Rh/Co
Co/Nb	0.044	—	—	0.066	—	—	0.065	—	—
Co09Rh/Nb	0.047	0.004	0.09	0.102	0.029	0.28	0.101	0.018	0.18
Co19Rh/Nb	0.043	0.008	0.19	0.081	0.037	0.46	0.080	0.023	0.29
Co24Rh/Nb	0.041	0.010	0.24	0.068	0.041	0.61	0.067	0.025	0.38
Co72Rh/Nb	0.044	0.032	0.72	0.093	0.111	1.20	0.091	0.068	0.74
Rh/Nb	—	0.011	—	—	0.039	—	—	0.024	—

Peak used for quantitation	B.E. (eV) (approx.)	Kinetic energy (eV)[a]	λ (nm)[b]	σ[c]
Co ($2p_{3/2}$)	779	708	2.55	12.62
Rh ($3d$)	308	1179	3.29	14.19
Nb ($3d$)	207	1280	3.44	8.21

[a] Calculated using the energy of the Al($K\alpha$) source (1487 eV).
[b] λ = electron attenuation length, from Seah and Dench equation for inorganic compounds (48).
[c] σ = X-ray photoionization cross section, from Scofield (49).

are the integrated signals of the Co ($2p_{3/2}$), Rh ($3d$), and Nb ($3d$) peaks, respectively, all taken at a pass energy of 150 eV. The "surface atomic ratio," determined from these XPS intensities, assumes the elements are homogeneously distributed in the XPS sampling depth (≈ 3.5 nm). The kinetic energies (KE), inelastic mean free paths (λ) and photoelectron cross-sections (σ) used in this analysis are also listed in Table 3. It is clearly seen that the catalyst surface is enriched with Rh and Co relative to Nb species for all samples, since their surface atomic ratios are ≈ two- to four-fold larger than their bulk atomic ratios. It is also clear that Rh is surface-enriched relative to Co, since the Rh/Co surface atomic ratios are larger than the bulk ratios by up to a factor of two.

4. ANALYSIS OF STRUCTURAL MODELS

Before proposing a structural model for these catalysts, some important experimental results should be reviewed. The TPR stoichiometries showed that the forms of Co and Rh are close to Co_3O_4 and Rh_2O_3, while the TPR lineshapes suggested the intimate interaction of the supported oxides of Co and Rh. Specifically, the Co_3O_4 reduction is greatly influenced by the presence of Rh, although the Rh_2O_3 reduction is relatively uninfluenced by the presence of Co (44). XPS lineshapes have shown the clear presence of two Co forms on the calcined surface (Co_3O_4 and Co^{+2} species). Through XPS intensities it was revealed that the Co and Rh oxides were preferentially located on the surface of the Nb_2O_5 support. These qualitative TPR and XPS observations provide enough information to postulate several model structures representing the surface of the calcined catalyst particles studied here, and to rule out other models. Below, we will use the quantitative XPS intensity ratios to eliminate certain models of the calcined catalysts, and to refine the models which do accurately describe the catalysts. First, we will describe the models considered for the structure of the catalysts.

4.1. Model for the Nb_2O_5 Support

The Nb_2O_5 support was found to be macroporous. For simplicity in modeling XPS intensities, we assumed that the support particles are composed of Nb_2O_5 spheres with a fixed diameter of 60 nm. The value of 60 nm was determined from matching the specific surface area of such spheres to the experimentally observed BET value of approximately 25 m^2/g. This diameter is much more than the attenuation length of photoelectrons (<4 nm), so the attenuation of photoelectrons originating from one "sphere" by other "sphere" was considered to be complete. That is, the observed photoelectrons were assumed to arise from spheres on the very surface of the powder as mounted. In effect, this means that the XPS intensities could be modeled by considering the photoelectron emission from the front face only of a single sphere of 60 nm diameter.

4.2. Models for the Calcined Bimetallic Catalysts

The simplest model would be a homogeneous mixture of Nb_2O_5, Co_3O_4, and Rh_2O_3. This, however, is clearly

ruled out by XPS, which shows the surface is enriched in Rh and, to a lesser extent, Co (see Table 3). The next simplest model would be a homogeneous Co_3O_4/Rh_2O_3 mixture uniformly spread as a film over the surface of the Nb_2O_5 support particles in a film of uniform thickness t. This is ruled out by the weak influence of Co on the Rh_2O_3 TPR and the presence of two forms of Co detected by XPS. The XPS Co/Nb, Rh/Nb, and Rh/Co ratios predicted by such a model were also markedly different from the experimental XPS ratios (seen in Table 3) by factors of 3.7–5.5, 1.3–2.8, and 0.36–0.69, respectively (depending on the Rh content of the catalysts). A description of the mathematical equations used for calculating the XPS intensities for this and all the models is given in the Appendix.

Next, we assumed a film containing a homogeneous mixture of Co_3O_4 and Rh_2O_3 was covering only a fraction f of the surfaces of the Nb_2O_5 particles, now in islands of uniform thickness t. We call this the "homogeneous islands" model. Again, for the same reasons, the TPR and XPS lineshapes ruled out such a model. This model also does not fit the XPS intensity data well at low Rh content, as shown in Fig. 5.

The filled data points of Fig. 5 show the relative errors in the XPS Co/Nb and Rh/Nb intensity ratios predicted by various models as a function of Rh content. These were calculated using the average-angle approximation, or Eq. [1a] in the Appendix, with $\theta = \theta_{av} = 57.3°$, and parameters that result in the best fit. Each one of these errors is defined as being the difference between the calculated and the experimental XPS intensity ratios relative to the experimental XPS intensity ratio. In all cases, the parameters within the model, such as f and t, were varied to minimize the sum of the squares of these two errors, subject to the constraint of maintaining the proper total amounts of Co, Rh, and Nb. This constraint means that certain parameters like f and t are not independent.

There are both filled and open data points in Fig. 5 for some of the catalysts and structural models. The additional *open* data points were calculated by using full angular integration, or Eq. [1c], but the same parameters as with the filled symbols. One can see that the average-angle approximation gives these XPS ratios for a given structure that are within 9% of those obtained by full integration.

A model wherein the Rh_2O_3 and Co_3O_4 existed only in separate islands on the support was also considered. It is obvious that such a model could easily fit the XPS intensities, since the thicknesses of the separate islands could simply be adjusted to give the proper signals. However, this model was ruled out by the strong influence of Rh on the TPR of the bimetallic Co–Rh oxides catalysts, which should not be so strong if the Rh and Co phases were well separated on the support. Such a model is also ruled out by the fact that it does not properly include a second Co species, of +2 character.

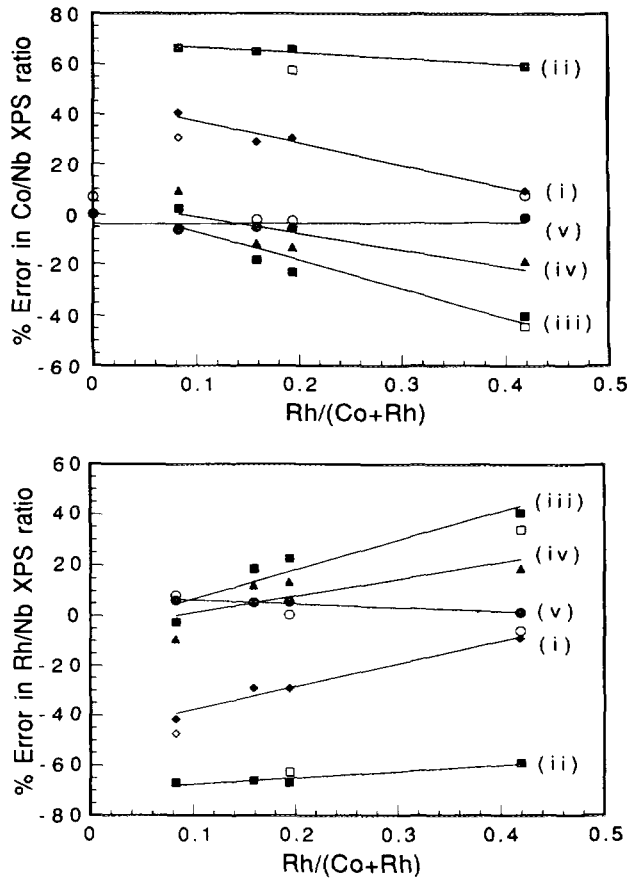

FIG. 5. Comparison of the structural models for calcined Co–Rh/Nb_2O_5 catalysts. The percentage errors in the calculated Co/Nb (a) and Rh/Nb (b) XPS intensity ratios, relative to the experimental values, are plotted as a function of the Rh content in the catalyst (on an atomic ratio basis). The calculated ratios of the Co/Nb and Rh/Nb XPS intensity plotted here as *filled* symbols are the ones obtained by using the average-angle approximation, or Eq. [1a] with $\theta = \theta_{av} = 57.3°$, and parameters that result in the best fit (i.e., the least sum of the squares of relative errors in the calculated Co/Nb *and* Rh/Nb ratios). The additional *open* data points were calculated by using these same parameters, but with full angular integration, or Eq. [1c]. Experimental errors in these ratios are estimated to be ~±8%. (i) Homogeneous islands of Co_3O_4 plus Rh_2O_3; (ii) bilayer islands with Co_3O_4 on top of Rh_2O_3; (iii) bilayer islands with Rh_2O_3 on top of Co_3O_4; (iv) bilayer islands with $CoRh_2O_4$ on top of Co_3O_4; and (v) bilayer islands with Rh_2O_3 on top of Co_3O_4 and with a surface Co^{+2} species in the areas between these islands. Model (v) is our preferred structural model, shown schematically in Fig. 6.

Models with the Rh and Co oxides in bilayer islands, covering a fraction f of the substrate, were considered next. Here, the Rh_2O_3 is assumed to be segregated either on the top of the Co_3O_4 or vice-versa, and each layer was assumed to be of uniform thickness. The "Co_3O_4-on top bilayer model" gave a poor fit to XPS intensities, as shown in Fig. 5. The "Rh_2O_3-on top bilayer model" fit

the XPS intensities reasonably well, although the error at high Rh content is unacceptable. Neither of these bilayer models properly account for a second Co species, as revealed by the Co (2*p*) XPS lineshape.

To incorporate two Co species, we considered models where the bilayer islands were composed of $CoRh_2O_4$ on top and Co_3O_4 below, covering a fraction *f* of the surface. (The stoichiometry of $CoRh_2O_4$ was chosen in the top layer, since this is a known Co^{+2} compound with known density (59).) In this model, we assumed that all of the Rh was in the form $CoRh_2O_4$. Quantitatively, this model fits the XPS intensities reasonably well (<19% error at all Rh contents). The thicknesses of the Co_3O_4 and $CoRh_2O_4$ layers predicted by this model were 0.14–0.32 nm and 0.04–0.23 nm, respectively, and these bilayer islands covered 4.0–7.6% of the support surface (depending on the Rh content). Despite these reasonable fits, this model was not preferred since the TPR showed that the Co had very little influence on the reduction of the Rh_2O_3, whereas the TPR of $CoRh_2O_4$ (16) is markedly different from that of Rh_2O_3 or any of the peaks seen in the TPR of the catalysts. However, the strongest reason to reject this model comes from the Co (2*p*) XPS lineshape of the monometallic Co/Nb catalyst that definitively showed the presence of two Co species, Co_3O_4 and Co^{+2}, despite the absence of Rh. This result shows that the Co^{+2} species is a result of Co–Nb_2O_5 interactions, and not Co–Rh interactions.

Finally, we considered a model with a Co^{+2} surface phase covering the surface of the Nb_2O_5 particles in the spaces between the bilayer islands. The structure of this model is represented in Fig. 6. The Co density in this Co^{+2} surface phase was assumed to be equal to that in bulk CoO, although this is not a critical assumption. (It only influences the final thickness of this Co^{+2} phase.) Again, the bilayer islands were assumed to cover a fraction *f* of the surface and consist of Rh_2O_3 on top of Co_3O_4. The thickness, t_i, for each phase, *i*, and the value of *f* which gave the best fit to the XPS intensities ratios (Co/Nb, Rh/Nb, and Co_3O_4/Co^{+2}) are tabulated for each catalyst in Table 4, along with the values calculated for these ratios. Their agreements with the measured ratios (presented in Table 3 and Fig. 4) are well within experimental error, as shown in Figs. 4 and 5. Note in Table 4 that, at all Rh contents, the thickness of the Co^{+2} phase is only 0.016–0.035 nm, showing that this phase is present at submonolayer concentrations, and could even be thought of as a Co^{+2} species absorbed on the Nb_2O_5 surface.

This model is our preferred structural description of the calcined Co–Rh/Nb_2O_5 catalysts. It has several advantages beyond fitting the XPS intensities. Such a surface phase of Co^{+2} oxide on Nb_2O_5 might be expected to resemble Co niobate ($CoNb_2O_6$), and indeed its Co (2*p*) lineshape in XPS resembles pure $CoNb_2O_6$, as was shown in Fig. 3b. Also, the amount of Co in this phase is very small, so that 78–90 wt% of the Co still resides in the Co_3O_4 phase (see Table 4, $\chi_{Co_3O_4}$). In the pure Co/Nb catalyst, 90 wt% of the Co is in the Co_3O_4 phase. Thus, the TPR should closely resemble that of pure Co_3O_4, as was observed (44). For the catalysts with Rh, the TPR still can be described as mainly resembling that of Co_3O_4, with the Co_3O_4 reduction catalyzed by the Rh overlayer. This results in the Co_3O_4 reduction peaks shifting to lower temperatures as Rh is added (44). The thin Co^{+2} surface phase, while quite obvious in XPS, arises from only a small fraction of the total Co present (10–15 wt%, depending on the Rh content), and therefore does not contribute significantly to the TPR profiles.

Another model which was considered involves *separate* islands of Rh_2O_3 and Co_3O_4, with the Co^{+2} surface phase in between. Perfect quantitative agreement with the XPS intensities can be achieved with this model,

TABLE 4

Parameters and Calculated XPS Ratios for the Preferred Structural Model: Bilayer Islands (Rh_2O_3 on top of Co_3O_4) with Co^{+2} Surface Phase

Sample	*f*	$t_{Co_3O_4}$ (nm)	$t_{Co^{+2}}$ (nm)	$t_{Rh_2O_3}$ (nm)	$\chi_{Co_3O_4}$	Theoretical XPS intensity ratios[a]			
						$I_{Co_3O_4}/I_{Co^{+2}}$	I_{Co}/I_{Nb}	I_{Rh}/I_{Nb}	I_{Rh}/I_{Co}
Co/Nb	0.013	9.08	0.016	0	0.90	0.922	0.070	0	—
Co09Rh/Nb	0.034	4.64	0.018	0.58	0.90	1.339	0.096	0.031	0.323
Co19Rh/Nb	0.031	4.29	0.017	0.88	0.89	1.042	0.079	0.039	0.494
Co24Rh/Nb	0.027	4.51	0.016	1.18	0.89	0.811	0.066	0.041	0.621
Co72Rh/Nb	0.044	2.84	0.035	2.56	0.78	0.251	0.099	0.105	1.061
Rh/Nb	0.015	0	0	3.10	0	—	0	0.037	—

[a] Calculated using full angular integration, Eq. [1c].

[b] $\chi_{Co_3O_4}$ is the weight fraction of the total Co present which is in the Co_3O_4 phase: ($\chi_{Co_3O_4} + \chi_{Co^{+2}} = 1.0$), where $\chi_{Co^{+2}}$ is the weight fraction of the total Co present which is in the Co^{+2} surface phase.

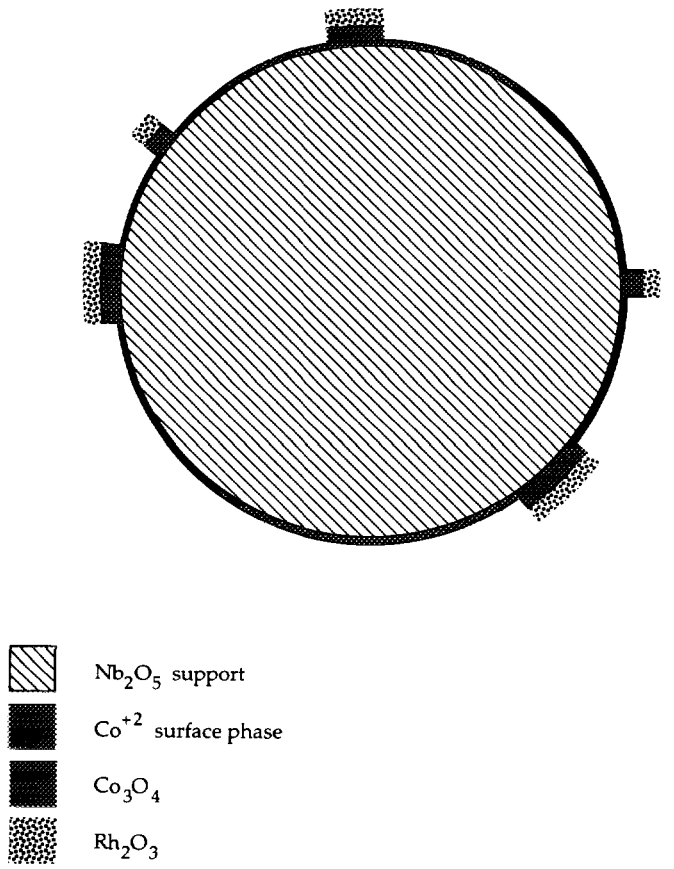

FIG. 6. Schematic representation of our preferred structural model for the calcined Co–Rh/Nb_2O_5 catalysts. This model has bilayer islands of Rh_2O_3 and Co_3O_4 covering a fraction f of the support surface, with Rh_2O_3 on top, and a highly dispersed Co^{+2} phase covering all regions in between these islands.

since it has one more adjustable parameter than the above model (the fraction covered by Rh_2O_3). In this model, the thicknesses and surface fractions covered by the various phases remains similar to those in Table 4, except that the fraction covered by Co_3O_4 is smaller than that shown, and these islands are thicker. (These differences are zero when Rh is absent, and they increase up to a factor of ≈5 at the highest Rh content.) Again, such a model was ruled out because of the strong influence of Rh on the TPR peak for the Co_3O_4 phase in these catalysts. We envision this arising from the acceleration of the dissociative adsorption of H_2 by the Rh metal. (Note that the Rh_2O_3 is reduced before the Co_3O_4.) This would clearly lead to accelerated Co_3O_4 reduction if the Rh_2O_3 sits on top of the Co_3O_4 islands, as in our preferred model. It could possibly also lead to acceleration of Co_3O_4 reduction if the Rh_2O_3 and Co_3O_4 were in separated islands and either the dissociated H could spill across the Co^{+2}-covered support to the Co_3O_4 particles or the Rh rapidly migrated over to the Co_3O_4 particles after Rh_2O_3 reduction. Since these possibilities cannot be excluded, such a model must be considered as a reasonable alternative to our preferred model. This alternative model, however, requires that the fraction of the surface covered by Co_3O_4 change by a factor of 3.7 with increasing Rh content for the bimetallic catalysts. If the Rh_2O_3 and Co_3O_4 were in *separate* islands, why should changing the Rh content in the supported phase from 8.3 to 41.9% (atomic basis) change the fraction covered by Co_3O_4 by a factor of nearly four? Note in Table 4 that this fraction is ≈0.036 and remains constant within ±25% as the Rh content increases in our preferred model for the bimetallic catalysts. It seems more reasonable that a *fixed* fraction of the support particles would offer surface facets that can be wetted by the Rh_2O_3/Co_3O_4 particles.

5. DISCUSSION

It is noteworthy in the preferred model of Fig. 6 and Table 4 that the fraction of the Nb_2O_5 surfaces which is covered by Rh_2O_3/Co_3O_4 bilayer islands, f, is rather small (≈3.6%). The Co^{+2} phase, on the other hand, is shown in Fig. 6 as covering the remainder of the surface in an extremely thin layer (0.016–0.035 nm). Since a monolayer of any Co^{+2} phase should be at least 0.3 nm thick, this apparent small thickness corresponds to a submonolayer phase of Co^{+2}, where only ≈5–12% of the remainder of the surface is actually covered by patches of single-monolayer thickness of the adsorbed Co^{+2} compound. Since the attenuation length, λ = 2.55 nm, of the Co(2p) line is considerably larger than the thickness of a monolayer (0.3–0.5 nm), we would also not be able to distinguish this from the similar models where this Co^{+2} phase was in thicker patches (up to ≈1.2 nm, or 3–4 monolayers) and covered even less of the surface. Other authors have postulated a highly dispersed surface phase of Co^{+2} on an Al_2O_3 support surface, together with separate thicker islands of Co_3O_4 for calcined Co/Al_2O_3 catalysts (monometallic (10, 28, 30) and promoted by Pt(10)) based on XPS (10, 30), TPR (28), XRD, Raman spectroscopy, and gravimetric analysis (30). The presence of a Co^{+2} species was previously detected on calcined Co/Nb_2O_5 catalysts based on DRS spectra, and XRD analysis of these catalysts were consistent with $CoNb_2O_6$ patterns. (However, the Co was mainly present as amorphous Co_3O_4 (40).)

This paper presents the first application of a new mathematical formalism (64) for modeling XPS intensities from supported bimetallic and multilayered catalysts. It integrates the emission of photoelectrons over the surface a hemisphere, whose radius is chosen to match the BET surface area. It assumes that this radius is large compared to the electron attenuation length, so it is appropriate only when this area is less than ~50 m^2/g. A

simple approximation to this formalism, using a planar model and an average take-off angle of photoelectrons from the local surface normal of 57.3°, is shown to be sufficient in many cases. For monometallic catalysts that do not cover a large fraction of the support, it gives results that agree within 9% of the randomly oriented hemispheres model of Kuipers *et al.* (65) (see Appendix). It is shown elsewhere (64) that this average-angle approach is inaccurate only when the signal from a species arises *mainly* from a phase that is buried more than two electron attenuation lengths below the surface. However, Kuipers' model is also in serious error in this case (64). Usually, this average-angle approach is far more accurate than simply assuming normal emission (64), as is frequently done (66).

6. CONCLUSION

Calcination at 673 K of a series of impregnated Co and Rh nitrates (at fixed Co content) supported on a Nb_2O_5 material leads to formation of the Co and Rh species identified as Co_3O_4, Co^{+2} phase, and Rh_2O_3. XPS, assisted by TPR data, has proven to be a powerful technique for ruling out several surface structural configurations of resulting bimetallic supported oxide catalysts, and for selecting one rather complex model which best describes the experimental data. This preferred model assumes bilayer islands of Rh_2O_3 on Co_3O_4 covering $\approx$3.6% of the Nb_2O_5 surface, with a highly-dispersed Co^{+2} surface phase in between these islands. The Co_3O_4 layers are $\approx$3–5 nm thick in these bilayer islands, and the Rh_2O_3 overlayer thickness increases with Rh content up to $\approx$3 nm. The model also showed that 78–90 wt% of the Co was present in the Co_3O_4 island layer. The Co^{+2} surface species does not require the presence of Rh_2O_3 to be readily formed on the Nb_2O_5 surface. However, a small amount of Rh_2O_3 added to the calcined Co/Nb_2O_5 catalyst significantly decreases the reduction temperature of the Co_3O_4 phase, as clearly observed by TPR, and consistent with this structural model. The new mathematical formalisms for quantitative XPS analysis proposed in (64) have proven here to be quite useful for bimetallic catalysts on supports whose BET areas are less than $\sim$50 m^2/g.

APPENDIX: XPS INTENSITY CALCULATIONS

The calculation of the XPS intensities for the various models followed a simple procedure. In the uniform film models, the known total Rh and Co contents allowed direct calculation of the film thickness t to match these contents, given the support radius of 30 nm. In models with islands, the fraction f of the support covered by each particular island type was first assumed. For models where all the Co exists in the Co_3O_4 phase, the thickness of the Co_3O_4 and Rh_2O_3 phases could again then be directly calculated to match the bulk Co and Rh contents. For models wherein some of the Co exists in another phase (either as $CoRh_2O_4$ or as a Co^{+2} surface phase), it was necessary to introduce the weight fraction of the total Co present which resides in the Co_3O_4 phase ($\chi_{Co_3O_4}$), in addition to the fraction of the support surface covered by the islands (f), before the thicknesses of the various phases could be calculated to give the known bulk concentrations of Co and Rh of each catalyst. The weight fraction $\chi_{Co_3O_4}$ was assumed for those models wherein the Co^{+2} surface phase was present, but it was forced to a fixed value in the model where all the Rh was assumed to be in the $CoRh_2O_4$ phase. In all cases, these assumed parameters (f, or f and $\chi_{Co_3O_4}$) were varied independently from 0.0 to 1.0, until the optimum fit to the measured XPS ratios was obtained.

In all models, the densities of the pure phase were taken from the literature (60), and mixed oxides were assumed to have the density of a weighted average of the two mixed phases. (For the model with a $CoRh_2O_4$ phase, its density was estimated from the crystallographic parameters of the spinel unit cell taken from the literature (59).)

The mathematical translation of the models starts with the traditional equation that describes the photoelectron intensity from a flat sample due to the integrated depth distribution of the element, weighted by the exponential decay of the escape probability of emitted photoelectrons with sampling depth (Eq. [1a]) (61–63). Thus, the integrated XPS intensity from the analysis area A on a flat sample for orbital j of element i is given by

$$I_{ij} = L_{ij}(\gamma)\,\sigma_{ij}\,K\,T(\mathrm{KE})\,A\int_0^\infty n_i(z)\,\exp[-z/(\lambda_{ij}(\mathrm{KE})\cdot\cos\theta)]\,dz, \qquad [1a]$$

where

$L_{ij}(\gamma)$ is the angular asymmetry factor of orbital j of element i;

σ_{ij} is the photoionization cross-section of orbital j of element i, taken from (49);

K is an instrumental constant which depends on the intensity and geometry of the X-ray source;

T(KE) is the transmission probability (including the detector efficiency) of the XPS analyzer, which is a smooth function of the kinetic energy (KE) of the emitted photoelectron, and which can depend on the geometry of the analyzer;

$n_i(z)$ is the atomic concentration of element i at depth z below the local surface (in units of atoms/cm^3);

λ_{ij}(KE) is the inelastic mean free path (IMFP) or attenuation length of a photoelectron from orbital j of element i

which is a function of the kinetic energy (KE) of the emitted photoelectron, taken from the Seah and Dench data (48) for inorganic compounds and oxides; and,

θ is the photoelectron take-off angle relative to the surface normal.

For our spectrometer and conditions of fixed pass energy, $T(\text{KE})$ is a constant for all elements (50). (While $K \cdot T(\text{KE}) \cdot A$ usually varies as $1/(\cos\theta)$ for flat samples and large-spot X-ray sources, it is independent of θ in our system even for flat samples because our X-ray spot is much smaller than the area imaged by the spectrometer.) Also, $L_{ij}(\gamma)$ is essentially unity for all elements when dealing with polycrystalline samples in spectrometers like ours which operate near the magic angle (61, 62).

We consider next support powders which can be modeled as a set of spheres whose effective diameter is much more than the IMFP of photoelectrons (typically 0.5–4 nm), so the attenuation of photoelectrons originating from one sphere by other sphere was considered to be complete. That is, the observed photoelectrons were assumed to arise from spheres on the very surface of the powder as mounted. In effect, this means that the XPS intensities could be modeled by considering the photoelectron emission from a single, isolated sphere of a typical effective diameter into an analyzer at infinite distance. In this case, the XPS intensity in Eq. [1a] above must be integrated over the volume of a spherical particle. Here, we will assume that the particle is so big that no electrons can get into the spectrometer if they originate from the back surface of the particle. Thus, this integral must only be performed over the front half of the hemisphere,

$$I_{ij} = K\,T(\text{KE})\,L_{ij}(\lambda)\,\sigma_{ij}\int_{r=0}^{R}\int_{\theta=0}^{\pi/2}\int_{\varnothing=0}^{2\pi} n_i(r)$$

$$\exp[-(R-r)/(\lambda_{ij}(\text{KE})\cdot\cos\theta)]\,r^2\sin\theta\,dr\,d\theta\,d\varnothing, \quad [1b]$$

where $\varnothing$ is the azimuthal take-off angle. The integral over this angle just gives 2π. We consider first only particles whose radius, R, is much, much larger than $\lambda_{ij}(\text{KE})$, so that the integral really need only be performed over a film of thickness equal to about $5\lambda_{ij}(\text{KE})$ on the surface of the particle. In this case, the integral can be replaced with

$$I_{ij} = K\,T(\text{KE})\,L_{ij}(\gamma)\,\sigma_{ij}\,2\pi R^2\int_{z=0}^{\infty}\int_{\theta=0}^{\pi/2} n_i(z)$$

$$\exp[-z/(\lambda_{ij}(\text{KE})\cdot\cos\theta)]\sin\theta\,dz\,d\theta, \quad [1c]$$

where $z = R - r$ is the depth below the local surface of the particle. For simplicity, we let its upper limit go to infinity rather than just to $5\lambda_{ij}(\text{KE})$, since the contribution to the integral between these limits is negligible (<1%).

We have recently shown (64) that, if $n_i(z)$ is a constant, N_i in some layer from z_1 to z_2 and zero elsewhere, then the double integral in Eq. [1c] simply equals

$$N_i \cdot \lambda_{ij}(\text{KE}) \cdot [E_3(z_1/\lambda_{ij}(\text{KE})) - E_3(z_2/\lambda_{ij}(\text{KE}))],$$

where $E_3(x)$ in the well-known and tabulated exponential integral function (67). We also presented a new approximate formula for evaluating $E_3(x)$ in (64). These simplifications are similar to the "randomly oriented hemispheres model" of Kuipers *et al.* (65), except that they are more accurate and applicable also to layered phases on the support, such as frequently occurs in bimetallic catalysts. They are used in evaluating Eq. [1c] here.

We have also recently shown (64) that Eq. [1c] for spherical particles can be accurately replaced by the much simpler Eq. [1a], provided that the properly averaged take-off angle for photoelectrons relative to the local surface normal is used for θ in the integral of Eq. [1a]. It turns out that the simple, unweighted, geometrically averaged take-off angle, $\theta_{av} = 57.3°$, gives intensity values which are within 9% of the full angular integration, Eq. [1c], over a very broad range of structural models (64). We have applied Eq. [1a] and used this value of θ_{av} in our calculations here, but only for optimizing structural parameters in the models. After the parameters were optimized, intensity ratios in the "best" model were also calculated using the full, angular-integrated Eq. [1c]. In all cases they were thus proven to be within good accuracy (see text). We also proved that this θ_{av} approximation gives XPS intensity ratios of Co/Nb and Rh/Nb for the preferred structural models of our monometallic catalysts that agreed within 9% of those predicted for these same models both by full integration or by the approximate integration method of Kuipers *et al.* (65).

For models where different depth distributions of the elements, $n_i(z)$, exist on different regions of the support particle surface, a sum of several $I_{ij}(k)$ terms is taken, using Eq. [1] for each

$$I_{ij}(\text{total}) = \sum_k f_k \cdot I_{ij}(k). \quad [2]$$

Here, f_k is the fraction of the support particle covered by region k, and $\Sigma_k f_k = 1.0$.

In our models, there are three regions at most: one or two covered by Co or Rh oxides, or by both, in islands, and another much larger region of either clean Nb_2O_5 or Nb_2O_5 covered by a thin Co^{+2} surface phase. Within any phase, $n_i(z)$ is a constant, so the depth distribution is defined by the phase thicknesses, t.

Simple geometric formulas relate the thicknesses of phases and the surface fraction coverage with the total amounts of Co and Rh present in the catalyst. For example, for the preferred model one may write

Co/Nb bulk atomic ratio

$$= \frac{(n_{Co_3O_4} \cdot V_{Co_3O_4} + n_{Co^{+2}} \cdot V_{Co^{+2}})}{n_{Nb_2O_5} \cdot V_{Nb_2O_5}}, \quad [3]$$

Rh/Nb bulk atomic ratio

$$= \frac{n_{Rh_2O_3} \cdot V_{Rh_2O_3}}{n_{Nb_2O_5} \cdot V_{Nb_2O_5}}, \quad [4]$$

where

$n_{Co_3O_4}$ is the Co atomic concentration (atoms/cm^3) in Co_3O_4;

$n_{Rh_2O_3}$ is the Rh atomic concentration (atoms/cm^3) in Rh_2O_3;

$n_{Nb_2O_5}$ is the Nb atomic concentration (atoms/cm^3) in Nb_2O_5;

$n_{Co^{+2}}$ is the Co atomic concentration (atoms/cm^3) in the Co^{+2} surface phase (taken equal that in bulk CoO).

$V_{Rh_2O_3}$ is the total bulk volume of Rh_2O_3 (in cm^3);

$V_{Co_3O_4}$ is the total bulk volume of Co in the Co_3O_4 phase (in cm^3);

$V_{Co^{+2}}$ is the total bulk volume of Co in the Co^{+2} surface phase (in cm^3); and

$V_{Nb_2O_5}$ is the total bulk volume of Nb_2O_5 (in cm^3);

The volumes of each phase are given by

$$V_{Rh_2O_3} = f(4/3)\pi[(r_{Rh_2O_3})^3 - (r_{Co_3O_4})^3], \quad [5]$$

$$V_{Co_3O_4} = f(4/3)\pi[(r_{Co_3O_4})^3 - (r_{Nb_2O_5})^3], \quad [6]$$

$$V_{Co^{+2}} = (1 - f)\,(4/3)\pi[(r_{Co^{+2}})^3 - (r_{Nb_2O_5})^3], \quad [7]$$

$$V_{Nb_2O_5} = (4/3)\pi(r_{Nb_2O_5})^3, \quad [8]$$

and their thicknesses are given by

$$t_{Rh_2O_3} = r_{Rh_2O_3} - r_{Co_3O_4}, \quad [9]$$

$$t_{Co_3O_4} = r_{Co_3O_4} - r_{Nb_2O_5}, \quad [10]$$

$$t_{Co^{+2}} = r_{Co^{+2}} - r_{Nb_2O_5}, \quad [11]$$

where

f is the surface fraction of the Nb_2O_5 covered by the bilayer Rh/Co oxides islands;

$(1 - f)$ is the surface fraction of the Nb_2O_5 covered by the Co^{+2} surface phase;

$r_{Rh_2O_3}$ is the radius of the sphere formed by the Rh_2O_3 shell (in nm);

$r_{Co_3O_4}$ is the radius of the sphere formed by the Co_3O_4 shell (in nm);

$r_{Co^{+2}}$ is the radius of the sphere formed by the Co^{+2} surface phase shell (in nm);

$r_{Nb_2O_5}$ is the radius of the Nb_2O_5 particle ($r_{Nb_2O_5} \approx 30$ nm);

$t_{Rh_2O_3}$ is the thickness of the Rh_2O_3 shell (in nm);

$t_{Co_3O_4}$ is the thickness of the Co_3O_4 shell (in nm); and,

$t_{Co^{+2}}$ is the thickness of the Co^{+2} surface phase shell (in nm).

Based on Eqs. [1a] (using θ_{av}) and [2], the XPS intensity ratios for the peaks quantified under the experimental conditions of this study can be expressed as follows for this preferred model

$$\frac{I_{Rh}}{I_{Nb}} = \frac{f \cdot \sigma_{Rh} \int_0^{t_{Rh_2O_3}} n_{Rh_2O_3} \cdot \exp[-z/(\lambda_{Rh} \cdot \cos\theta_{av})]\,dz}{f \cdot \sigma_{Nb} \int_{t_{bilayer}}^{\infty} n_{Nb_2O_5} \cdot \exp[-z/(\lambda_{Nb} \cdot \cos\theta_{av})]\,dz + (1 - f) \cdot \sigma_{Nb} \int_{t_{Co^{+2}}}^{\infty} n_{Nb_2O_5} \cdot \exp[-z/(\lambda_{Nb} \cdot \cos\theta_{av})]\,dz} \quad [12]$$

and

$$\frac{I_{Co}}{I_{Nb}} = \frac{f \cdot \sigma_{Co} \int_{t_{Rh_2O_3}}^{t_{bilayer}} n_{Co_3O_4} \cdot \exp[-z/(\lambda_{Co} \cdot \cos\theta_{av})]\,dz + (1 - f) \cdot \sigma_{Co} \int_0^{t_{Co^{+2}}} n_{Co^{+2}} \cdot \exp[-z/(\lambda_{Co} \cdot \cos\theta_{av})]\,dz}{f \cdot \sigma_{Nb} \int_{t_{bilayer}}^{\infty} n_{Nb_2O_5} \cdot \exp[-z/(\lambda_{Nb} \cdot \cos\theta_{av})]\,dz + (1 - f) \cdot \sigma_{Nb} \int_{t_{Co^{+2}}}^{\infty} n_{Nb_2O_5} \cdot \exp[-z/(\lambda_{Nb} \cdot \cos\theta_{av})]\,dz}, \quad [13]$$

where $t_{bilayer} \equiv t_{Co_3O_4} + t_{Rh_2O_3}$.

These equations can be integrated and simplified to give

$$\frac{I_{Rh}}{I_{Nb}} = \frac{S_{Rh}}{S_{Nb}} \times \frac{n_{Rh_2O_3}}{n_{Nb_2O_5}} \times \frac{f\{1 - \exp[-t_{Rh_2O_3}/(\lambda_{Rh} \cdot \cos\theta_{av})]\}}{f \cdot \exp[-t_{bilayer}/(\lambda_{Nb} \cdot \cos\theta_{av})] + (1 - f) \cdot \exp[-t_{Co^{+2}}/(\lambda_{Nb} \cdot \cos\theta_{av})]} \quad [14]$$

$$\frac{I_{Co}}{I_{Nb}} = \frac{S_{Co}}{S_{Nb}} \times \frac{A_{Co_3O_4} + A_{Co^{+2}}}{n_{Nb_2O_5}\{f \cdot \exp[-t_{bilayer}/(\lambda_{Nb} \cdot \cos\theta_{av})] + (1 - f) \cdot \exp[-t_{Co^{+2}}/(\lambda_{Nb} \cdot \cos\theta_{av})]\}} \quad [15]$$

where S_i is the bulk sensitivity factor for the peak of element i, defined as $S_i \equiv \sigma_i \times \lambda_i$; $A_{Co_3O_4} \equiv n_{Co_3O_4}\{f[\exp(-t_{Rh_2O_3}/(\lambda_{Co} \cdot \cos\theta_{ab})) - \exp(-t_{bilayer}/(\lambda_{Co} \cdot \cos\theta_{av}))]\}$; and $A_{Co^{+2}} \equiv n_{Co^{+2}}\{(1-f)[1 - \exp(-t_{Co^{+2}}/(\lambda_{Co} \cdot \cos\theta_{av}))]\}$.

By looking at Eq. [15], one can seen that the Co XPS signal arises from the sum of two terms: one due to the Co^{+2} surface phase and the other due to the Co_3O_4 phase. The ratio of these signals is just

$$\frac{I_{Co_3O_4}}{I_{Co^{+2}}} = \frac{n_{Co_3O_4}}{n_{Co^{+2}}} \times \frac{f[\exp(-t_{Rh_2O_3}/(\lambda_{Co} \cdot \cos\theta_{av})) - \exp(-t_{bilayer}/(\lambda_{Co} \cdot \cos\theta_{av}))]}{(1-f)[1 - \exp(-t_{Co^{+2}}/(\lambda_{Co} \cdot \cos\theta_{av}))]}. \quad [16]$$

For all of the preferred models, and for many of the other models, we also evaluated the equivalent of Eqs. [12]–[16] using the full, angular-integrated Eq. [1c] instead of [1a], and we found the XPS ratios to agree within experimental error in all cases. The ratios calculated within this more accurate method for the optimum parameters of this model are tabulated in Table 4 for comparison to the experimental data. This Co_3O_4/Co^{2+} ratio is plotted in Fig. 4 for comparison to the experimental data.

ACKNOWLEDGMENTS

The authors thank the technical assistance of Mrs. Deborah Leach-Scampavia. We also thank the editor, Nick Delgass, and two conscientious referees for very helpful comments. Financial support for this research by the Department of Energy, Office of Basic Energy Sciences, Division of Chemical Sciences is gratefully acknowledged by C. T. C.. A. F. thanks the CNPq (Conselho Nacional de Desenvolvimento Científico e Tecnológico), of the Secretary for Science and Technology of Brasil, for the scholarship granted to pursue a split fellowship program at the University of Washington. A. F. thanks Mr. R. R. Soares for providing cobalt niobate samples.

REFERENCES

1. Anderson, R. B., "The Fischer-Tröpsch Synthesis." Academic Press, Orlando, 1984.
2. Bhasin, M. M., Bartley, W. J., Ellgen, P. C., and Wilson, T. P., *J. Catal.* **54,** 120 (1978).
3. The Research Association for C_1 Chemistry, "Progress in C_1 Chemistry in Japan." Kodansha, Tokyo, 1989.
4. Herman, R. G., *in* "New Trends in CO activation (Stud. Surf. Sci. Catal.)" (L. Guczi, Ed.), Vol. 64, p. 265. Elsevier, Amsterdam, 1991.
5. Kunimori, K., Arakawa, H. and Uchijama, T., *in* "Future Opportunities in Catalytic and Separation Technology (Stud. Surf. Sci. Catal.)" (M. Misono et al., Eds.), Vol. 54, p. 144. Elsevier, Amsterdam, 1989.
6. Sinfelt, J. H., "Bimetallic Catalysts—Discoveries, Concepts and Applications," Wiley, New York, 1983.
7. Goodwin Jr., J. G., *in* "Proceedings of The Symposium on Methane Upgrading," ACS, p. 156. Atlanta, 1991.
8. Guczi, L., Matusek, K., Bogyay, I., Garin, F., Puges, P. E., Girard, P., and Maire, G., *C_1 Mol. Chem.* **1,** 355 (1986).
9. Dees, M. J., Shido, T., Iwasawa, Y., and Ponec, V., *J. Catal.* **124,** 530 (1990).
10. (a) Zsoldos, Z., Hoffer, T., and Guczi, L., *J. Phys. Chem.* **95,** 798 (1991); (b) Guczi, L., Hoffer, T., Zsoldos, Z., Zyade, S., Maire, G., and Garin, F., *J. Phys. Chem.* **95,** 802 (1991); (c) Zsoldos, Z., and Guczi, L., *J. Phys. Chem.* **96,** 9393 (1992).
11. Iglesia, E., Stuart, L. S., Rocco, A. F., and Grayson, H. V., *J. Catal.* **143,** 345 (1993).
12. Matsuzaki, T., Takeuchi, K., Hanaoka, T., Arakawa, H., and Sugi, Y., *Appl. Catal.* **105,** 159 (1993).
13. Ladner, W. R., and Richards, D. G., *in* "Proceedings of the International Conference on Coal Science," p. 335. Pergamon, Sydney, 1985.
14. Villeger, P., Barrault, J., Barbier, J., Leclerq, G., and Maurel, R., *Bull. Soc. Chim. Fr.*, I-413 (1979).
15. Ichikawa, M., *J. Catal.* **56,** 127 (1979).
16. Van't Blik, H. J. F., Ph.D. Thesis, University of Technology, Eindhoven, 1984.
17. Vannice, M. A., *J. Catal.* **37,** 449 (1975).
18. Vannice, M. A., *J. Catal.* **50,** 228 (1977).
19. Zowtiak, J. M., and Bartholomew, C. H., *J. Catal.* **83,** 107 (1983).
20. Reuel, R. C., and Bartholomew, C. H., *J. Catal.* **85,** 63 (1984).
21. Castner, D. G. and Santilli, D. S., *in* "Catalytic Materials: Relationship Between Structure and Reactivity (ACS Symposium Series)" (T. E. White, Jr., R. A. Dalla Betta, E. G. Derouane, and R. T. K. Baker, Eds.), Vol. 248, p. 39. 1984.
22. Lapidus, A. L., Krylova, A. Yu., Rathousky, J., Zukal, A. and Jancálková, M., *Appl. Catal.* **80,** 1 (1992).
23. Lee, J. H., Lee, D. K., and Ihm, S. K., *J. Catal.* **113,** 544 (1988).
24. Palmer, R. L., and Vroom, D. A., *J. Catal.* **50,** 244 (1977).
25. Ignatiev, A., and Matsuyama, T., *J. Catal.* **58,** 328 (1979).
26. LoJacono, M. Schiavello, M., and Cimino, C., *J. Phys. Chem.* **75,** 1044 (1971).
27. Chin, R. L., and Hercules, D. M., *J. Phys. Chem.* **86,** 360 (1982).
28. Arnoldy, P., and Moulijn, J. A., *J. Catal.* **93,** 38 (1985).
29. Chung, K. S., and Massoth, F. E., *J. Catal.* **64,** 322 (1980).
30. (a) Stranick, M. A., Houalla, M., and Hercules, D. M., *J. Catal.* **103,** 151 (1987); (b) Stranick, M. A., Houalla, M., and Hercules, D. M., *J. Catal.* **106,** 362 (1987); (c) Stranick, M. A. Houalla, M., and Hercules, D. M., *J. Catal.* **125,** 214 (1990).
31. Fu, L., and Bartholomew, C. H., *J. Catal.* **92,** 376 (1985).
32. Reuel, R. C., and Bartholomew, C. H., *J. Catal.* **85,** 78 (1984).
33. Derule, H., Blanchard, M., and Canesson, P., *Appl. Catal.* **50,** L1 (1989).
34. Hutchings, G. J., Van der Riet, M., and Hunter, R., *J. Am. Chem. Soc., Faraday Trans. 1* **85**(9), 2875 (1989).
35. Forzatti, P., Tronconi, E., and Pasquon, I., *Catal. Rev.-Sci. Eng.* **32**(4), 279 (1991).
36. Burch, R., and Petch, M. I., *Appl. Catal.* **88,** 39 (1992).
37. Silva, R. R. C. M., Schmal, M., Frety, R., and Dalmon, J. A., *J. Chem. Soc., Faraday Trans.* **89**(21), 3975 (1993).
38. Macedo, J. C. D., Schmal, M., and Dalmon, J. A., *in* "Proceedinds of The X Iberoamerican Symposium on Catalysis," Vol. 2, p. 666. 1986.
39. Frydman, A., Soares, R. R., and Schmal, M., *in* "New Frontiers in Catalysis (Stud. Surf. Sci. Catal.)" (B. Delmon and J. T. Yates, Eds.), Vol. 75, p. 2796. Elsevier, Amsterdam, 1993.
40. Soares, R. R., Frydman, A., and Schmal, M., *Catal. Today* **16,** 361 (1993).

41. Iizuka, T., Tanaka, Y., and Tanabe, K., *J. Mol. Catal.* **17,** 381 (1982).
42. Vannice, M. A., and Garten, R. L., *J. Catal.* **56,** 236 (1979).
43. Ko, E. I., and Hupp, M., *J. Catal.* **86,** 315, 1984.
44. Frydman, A., Castner, D. G., Campbell, C. T., and Schmal, M., to be published.
45. Ko, E. I., and Weissman, J. G., *Catal. Today* **8,** 27 (1990).
46. Gomes, M. F. T., and Eon, J. G., "Proceedings of The XII Symposium Iberoamerican on Catalysis," p. 176. 1990.
47. Barth, G., Linder, R., and Bryson, C., "Advances in Charge Neutralization for XPS Measurements of Nonconducting Materials," Surface and Interface Analysis, Vol. 11, p. 307. 1988.
48. Seah, M. P., and Dench, W. A., *Surf. Interface Anal.* **1**(1), 2 (1979).
49. Scofield, J. H., *J. Electron Spectrosc. Relat. Phenom.* **8,** 129 (1976).
50. "Transmission-function Characterization", application note from Surface Science Instruments, Moutain View, CA, 1987.
51. Brown, R., Cooper, M. E., and Whan, D. A., *Appl. Catal.* **3,** 177 (1982).
52. Paryjczak, T., Rynkowski, J., and Karski, S., *J. Chromatogr.* **188,** 254 (1980).
53. Castner, D. G., Watson, P. R., and Chan, I. Y., *J. Phys. Chem.* **94,** 819 (1990).
54. Greenwood, N. N. and Earnshaw, A., "Chemistry of The Elements," p. 1290. Pergamon, Oxford, 1984.
55. (a) Nefedov, V. I., Firsov, M. N., and Shaplygin, I. S., *J. Electron. Spectrosc. Relat. Phenom.* **26,** 65 (1982); (b) Nefedov, V. I., Gati, D., Dzhurinskii, B. F., Sergushin, N. P., and Salyn, Y. V., *Zh. Neorg. Khim.* **20,** 2307 (1975); (c) Garbassi, F., Bart, J. C. J., and Petrini, G., *J. Electron. Spectrosc. Relat. Phenom.* **22,** 95 (1981); (d) Nefedov, V. I., Salyn, Y. V., Chertkov, A. A., and Padurets, L. N., *Zh. Neorg. Khim.* **19,** 1443 (1974); (e) Bahl, M. K., *J. Phys. Chem. Solids* **36,** 485 (1975); (f) Simon, D., Perrin, C., and Baillif, P., C. R. *Acad. Sci. Ser. C* **283,** 241 (1976); (g) McGuire, G. E., Schweitzer, G. K., and Carlson, T. A., *Inorg. Chem.* **12,** 2451 (1973); (h) Fontaine, R., Caillat, R., Feve, L., and Guittet, M. J., *J. Electron. Spectrosc. Relat. Phenom.* **10,** 349 (1977); (i) Sarma, D. D., and Rao, C. N. R., *J. Electron. Spectrosc. Relat. Phenom.* **20,** 25 (1980).
56. (a) Chuang, T. J., Brundle, C. R., and Rice, D. W., *Surf. Sci.* **59,** 413 (1976); (b) Wagner, C. D., Riggs, W. M., Davis, L. E., Moulder, J. F., and Muilenberg, G. E., "Handbook of Xray Photoelectron Spectroscopy," Perkin–Elmer Corporation, Minnesota, 1979; (c) Okamoto, Y., Imanaka, T., and Teranishi, S., *J. Catal.* **65,** 448 (1980); (d) Gajardo, P., Pirotte, D., Defosse, C., Grange, P., and Delmon, B., J. Electron Spectrosc. Relat. Phenom. **17,** 121 (1979); (e) Oku, M. and Hirokawa, K., *J. Electron Spectrosc. Relat. Phenom.* **8,** 475 (1976); (f) Schenck, C. V., Dillard, J. G., and Murray, J. W., *J. Colloid Interface Sci.* **95,** 398 (1983).
57. (a) Okamoto, Y., Ishida, N., Imanaka, T., and Teranishi, S., *J. Catal.* **58,** 82 (1979); (b) Contour, J. P., Mouvier, G., Hoogewijs, M., and Leclerq, C., *J. Catal.* **48,** 217 (1977); (c) Andersson, S. L. T., Watters, K. L., and Howe, R. F., *J. Catal.* **69,** 212 (1981).
58. (a) Dennis, A. M., Howard, R. A., Kadish, K. M., Bean, J. L., Brace, J., and Winograd, N., *Inorg. Chim. Acta* **44,** L139 (1980); (b) Wehner, P. S., Mercer, P. N., and Apai, G., *J. Catal.* **84,** 244 (1983); (c) Friedman, R. M., Hudis, J., Perlman, M. L., and Watson, R. E., *Phys. Rev. B* **8,** 2434 (1973).
59. Bertaut, F., Forrat, F., and Dulac, J., *C. R. Hebdomadaires Seances L'Acad. Sci.* **249,** 726 (1959).
60. "Handbook of Chemistry and Physics," R. C. Weast, Ed., 49th ed., The Chemical Rubber Co., Cleveland, 1968.
61. Ratner, B. D., and Castner, D. G., submitted for publication.
62. Ertl, G., and Küppers, J., "Low Energy Electrons and Surface Chemistry," 2nd ed. VHC, Verlagsgesellschaft, Weinheim, 1985.
63. "Practical Surface Analysis," D. Briggs and M. P. Seah, Eds., Vol. 1, 2nd ed., Wiley, Chichester, 1990.
64. Frydman, A., Castner, D. G., Schmal, M., and Campbell, C. T., submitted for publication to *J. Catal.*
65. Kuipers, H. P. C. E., van Leuven, H. C. E., and Visser, W. M., *Surf. Interface Anal.* **8,** 235 (1986).
66. Kerkhoff, F. P. J. M., and Moulijn, J. A., *J. Phys. Chem.* **83,** 1612 (1979).
67. Abramovich, M., and Stegun, I. A. (Eds.), "Handbook of Mathematical Functions," U.S. National Bureau of Standards, Applied Mathematics Series Vol. 55, pp. 228–248. U.S. Govt. Printing Office, Washington, D.C., 1972.